Vibration Performance of A Flow Energy Converter behind Two Side-by-Side Cylinders

Mohammad Rasidi Rasani*
Center for Integrated Design for Advanced Mechanical Systems,
Faculty of Engineering and Built Environment,
Universiti Kebangsaan Malaysia, Bangi, 43600 Selangor, Malaysia;
rasidi@ukm.edu.my (MRR)

Hazim Moria
Department of Mechanical Engineering Technology,
Yanbu Industrial College,
46452 Yanbu Al-Bahr, Saudi Arabia;
moriah@rcyci.edu.sa (HM)

Michael Beer
Institute for Risk and Reliability,
Leibniz University Hannover,
30167 Hannover, Germany;
beer@irz.uni-hannover.de (MB)

Ahmad Kamal Ariffin
Center for Integrated Design for Advanced Mechanical Systems,
Faculty of Engineering and Built Environment,
Universiti Kebangsaan Malaysia, Bangi,
43600 Selangor, Malaysia;
kamal3@ukm.edu.my (AKA)

July 14, 2020

Abstract

Flow-induced vibrations of a flexible cantilever plate, placed in various positions behind two side-by-side cylinders, were computationally investigated to determine optimal location for wake-excited energy harvesters. In the present study, the cylinders of equal diameter D are fixed at center-to-center gap ratio of $T/D = 1.7$ and immersed in sub-critical flow of Reynold number

---

*correspondence:rasidi@ukm.edu.my

$Re_D = 10000$. A three-dimensional Navier-Stokes flow solver in an Arbitrary Lagrangian-Eulerian (ALE) description was closely coupled to a non-linear finite element structural solver that was used to model the dynamics of a composite piezoelectric plate. The cantilever plate was fixed at several positions between $0.5 < x/D < 1.5$ and $-0.85 < y/D < 0.85$ measured from the center gap between cylinders, and their flow-induced oscillations were compiled and analyzed. Results indicate that flexible plates located at the centerline between the cylinder pairs experience lowest mean in amplitude of oscillation. Maximum overall amplitude in oscillation is predicted when flexible plates are located in the intermediate off-center region downstream of both cylinders. Present findings indicate potential to further maximize wake-induced energy harvesting plates by exploiting their favourable positioning in the wake region behind two side-by-side cylinders.

1   Introduction

Flow around single or group of cylinders is a fundamental fluid dynamics problem that have attracted considerable research due to its wide engineering significance. Flow past a cylinder typically involves boundary layer separation/reattachments, free shear layers and vortex shedding, which induces cylinder vibrations and noise generation. These flow dynamics become more complicated when there are interference or interactions with neighbouring cylinders. The understanding behind such flow past multiple cylinders provide important insight as they are found in many branches of engineering applications for example - cooling cores in nuclear reactors, heat exchanger tube bundles, offshore structures, marine risers and pipelines. Among flow past multiple cylinders, the case involving two cylinders has been investigated both numerically and experimentally under several configurations, either in-tandem, side-by-side or staggered arrangements and provide some fundamental understanding of flow or wake interactions [1, 2].

Flow characteristics past two side-by-side cylinders are strongly influenced by the gap between cylinders and their diameter-based Reynolds number, Re_D. Denoting T as the transverse center-to-center distance between cylinders and D as the cylinder diameter, the flow behaviour around side-by-side cylinders may be classified into three main regimes [3, 4] : (i) When $T/D < 1.1 - 1.2$, the gap between cylinders is small and the flow behaves like passing a single bluff body where vortices are shed alternately from the outer surfaces of the top and bottom cylinders, forming an asymmetric single vortex street. In this single-bluff body regime, the Strouhal number ($St = f(2D)/U_\infty$) is approximately 0.2 - similar to a single-bluff body case, but with characteristic length of $2D$ [5]. (ii) When $1.2 < T/D < 2.0 - 2.2$, this intermediate spacing between cylinders is within a critical range where the flow between the gap is bistable and switches direction (flip-flopping) towards either cylinders at irregular intervals (with periods several orders of magnitude larger than the vortex shedding period). As a result, in this biased flow regime, a narrower and wider wake region forms behind either cylinders, corresponding to higher ($St_n \approx 0.2 - 0.4$) and

2

lower ($St_w \approx 0.1 - 0.2$) vortex shedding frequencies respectively [6]. Within this regime, the Reynolds number Re may also influence the transition between single and twin vortex streets [7, 8]. In their 3-D numerical study, Liu et al. [9] also showed the influence of cylinder inclination (or conversely, flow angle) on formation of these vortex streets. (iii) When $T/D > 2.2$, the gap is sufficiently large that both cylinders behaves more like isolated bluff bodies resulting in a predominantly symmetric (or anti-phase) parallel wake patterns, that are coupled with a single Strouhal number St of approximately 0.21 [6]. Intermittent in-phase wake patterns may also take place in this symmetric flow regime, but would then synchronizes back to the more stable anti-phase or symmetric pattern. At much higher gaps ($T/D > 4.5$), any interference associated with proximity of cylinders are negligible and each cylinder behaves as independent bluff bodies with uncoupled flow patterns [3].

Previous studies on flow around bluff bodies with adjacent plates may also provide useful context for the present work. Flow past a single cylinder with plates have received much attention in the past decades, especially for passive flow/vortex control (and subsequently, flow-induced vibration control) of a cylinder (see for example, [10, 11, 12, 13]), understanding of plate dynamics (for instance, [14, 15]) and potential for energy harvesting (see for example, [16, 17]). Less well explored are flow with plates behind two or multiple cylinders. Furquan et al. [18] computationally investigated vibration response of two flexible splitter plates, each placed behind two side-by-side square cylinders (that are separated by center-to-center distance equal to twice the square edge length L) at $Re = 100$ under varying reduced velocities ($U^* = U_\infty/f_n L$ where f_n is plate natural frequency). Their results indicate initial anti-phase plate vibration as the plates are attracted towards each other with the accelerating gap flow, before finally synchronizing into an in-phase plate vibration pattern that also exhibits the 'lock-in' phenomena at certain range of U^*, as either plates undergo large vibration amplitudes when their response frequency approaches the plate first mode natural frequency. Effect of short splitter plates behind two side-by-side square cylinders (with center-to-center distance equal 3.6 times the square edge length) on their vortex shedding and subsequent sound generation were examined experimentally for Re between 10000-33000 by Octavianty and Asai [19]. In this symmetric flow regime and high Re, generated vortices past the side-by-side square cylinders were highly synchronized and coherent span-wise, allowing effective sound reduction even with shorter splitter plates - in contrast to a single square cylinder where vortices were more three-dimensional and effect of splitter plate was limited. Oruc et al. [20] experimented with splitter plates centrally placed between two side-by-side circular cylinders and examined their effect on the flip-flopping gap flow in the biased flow regime. It was found that at sufficient plate lengths, the asymmetric and bistable wake flow were suppressed, resulting in two symmetric and stable wake patterns.

Demand for clean and sustainable energy that requires minimal human intervention or maintenance (for example, to power wireless sensors in remote areas, electronic devices for structural health monitoring of airborne vehicles or deep ocean structures) have prompted increasing development of various energy harvesting systems. One of a number of prototypes include exploiting wakes behind a single bluff body (for example, [21, 17, 16, 22]) and wake-induced vibration of cylinders (for example, [23]) to induce oscillations of flexible membranes or plates consisting of piezoelectric materials - converting

the fluctuating mechanical strains or energy into electrical energy and have been shown to reach outputs up to 30V [24, 25]. Although multiple bluff bodies are ubiquitous in many engineering applications, limited investigation on their potential to excite piezoelectric energy harvesters may be found.

Therefore, in the present study, we aim to extend the current results in the literature by exploring wake-excited piezoelectric energy harvesters placed behind two side-by-side cylinders and also analyze their vibrations at various placements in the wake region with the view of maximizing energy harvesting performance. To that end, we performed computational investigation on unsteady flow past two side-by-side circular cylinders interacting with a thin flexible plate placed at a number of streamwise and crossflow positions behind both cylinders. As the side-by-side cylinders behave like a single bluff body, either in unison or separated when the gap is small or large enough respectively, we considered a center-to-center cylinder spacing of $T/D = 1.7$ (in the bias flow regime) for the present study, to include effects of multiple bluff body flow interaction or interference. In addition, a moderately high sub-critical flow past cylinders of $Re_D = 10000$ is considered in the present work.

2 Computational Methodology

2.1 Flow Equations

Although vortex shedding behind a circular cylinder may be initiated at $Re_D \approx 49$, numerous bluff-body energy harvesting prototypes suggest operations at much higher Reynolds numbers (for example, $Re_D = 5000 - 40000$ for harvesting eel of Allen and Smits [21], $Re_D = 3000 - 8000$ for harvesting concept in Weinstein et al. [26], $Re_D = 6024$ for proposed miniature energy generator in Nguyen et al. [27], Re_D in excess of 10000 in the investigation by Yu and Liu [16] and Re_D ranging between 3200 to 12000 in the design by Shi et al. [17]). As a result, we consider $Re_D = 10000$ in the present study, which falls in the sub-critical flow regime of flow past circular cylinders. Within this regime, flow is three-dimensional and boundary layers remain laminar prior to separation, which then becomes turbulent in the wake region. In order to better simulate flow separation and turbulence but with more practical computational cost, a recently developed Scale-Resolving or Scale-Adaptive Simulation (SAS) modification on the $k - \omega$ Shear Stress Transport (SST) turbulence model proposed by Menter and Egorov [28] was employed. This involves the incompressible, three-dimensional Unsteady Reynolds-Averaged Navier Stokes (URANS) equation for conservation of momentum and the continuity equations, both of which in this case are described in the Arbitrary Lagrangian-Eulerian (ALE) frame of reference in order to accommodate fluid grid movements or deformation, as the grids follow the motion of the interfacing flexible plate [29, 30]:

$$\frac{\partial u_i}{\partial t} + (u_j - \widetilde{u}_j)\frac{\partial u_i}{\partial x_j} = -\frac{1}{\rho}\frac{\partial p}{\partial x_i} + \frac{1}{\rho}\frac{\partial}{\partial x_j}\left\{(\mu + \mu_t)\left(\frac{\partial u_i}{\partial x_j} + \frac{\partial u_j}{\partial x_i}\right)\right\} \qquad (1)$$

$$\frac{\partial(u_i - \widetilde{u}_i)}{\partial x_i} = 0 \qquad (2)$$

4

where u_i, $\widetilde{u}_j$ and p are the time-averaged fluid velocities, fluid grid velocities and time-averaged fluid pressure respectively ($i, j = 1, 2, 3$ represent the 3-D cartesian directions). ρ is the constant fluid density, μ denotes the fluid dynamic viscosity and μ_t is the turbulent eddy viscosity. In the $k - \omega$ SST model, μ_t is estimated from the turbulent kinetic (k) energy and specific rate of dissipation (ω) equations. SAS treatment of the $k - \omega$ shear stress transport turbulence model estimates a von Kármán length-scale and introduces a corresponding source term into the ω equation, allowing the model to switch between RANS and LES-like simulations [28, 31]. Thus, more unsteady turbulent structures are able to be resolved as mesh is refined, but at lower computational costs compared to LES or DNS simulations. Fluid grid velocities are solved using a Laplacian Diffusion model, which smoothly distributes the grid velocities in the whole fluid domain, from a value matching the plate motion near the fluid-plate interface, to zero at the fluid domain boundaries.

2.2 Structural Equations

The flexible plate dynamics is described by the unsteady equation of motion in Eq. (3).

$$\rho_s \ddot{\mathbf{d}} = \nabla \cdot \sigma_{ij} + \mathbf{f} - c\dot{\mathbf{d}} \tag{3}$$

where σ_{ij} is the stress tensor and the first term on the right-hand side accounts for the stiffness of the structure, allowing for non-linear large plate deformation and accounting for the effect of induced in-plane tension on bending deflection. In addition, c represents damping ratio, ρ_s denotes density of structure material, $\mathbf{d}$ represents displacement vector of structure and $\mathbf{f}$ represents a time-dependent external force acting on structure (coming from the interfacing fluid pressure and shear). In the present work, we considered neglecting structural damping.

2.3 Computational Model

Figure 1 shows the computational domain used in the present study, which spans $30D \times 16D \times 1D$ in the streamwise (x), crossflow (y) and spanwise (z) directions respectively. The inlet and outlet boundaries are respectively located $10D$ upstream and $20D$ downstream of the side-by-side cylinders. As the cylinder centers are spaced $T/D = 1.7$ apart, we employed a symmetrical height of $8D$ from either top and bottom boundaries to the middle of the gap between cylinders. In addition, a spanwise width of $1D$ was considered in the present domain. Studies by Alkishriwi et al. [32] and Shen et al. [33] showed that results with spanwise width of $1D$ agreed well with experiments. Table 1 summarizes the geometrical parameters employed in the present study for both fluid and structural components.

Boundary conditions prescribed in the computational domain are shown in Figure 1. In addition, both left and right faces of the fluid domain are defined as symmetric conditions and both cylinder surfaces are prescribed as no-slip walls. The fluid faces that interface with the flexible plate are also specified as no-slip walls, implying a dynamic condition that requires matching fluid and plate velocities at these boundaries. For the structural domain, the leading edge of the cantilever flexible plate is fixed, while both left and right side faces of the plate are prescribed as symmetric conditions.
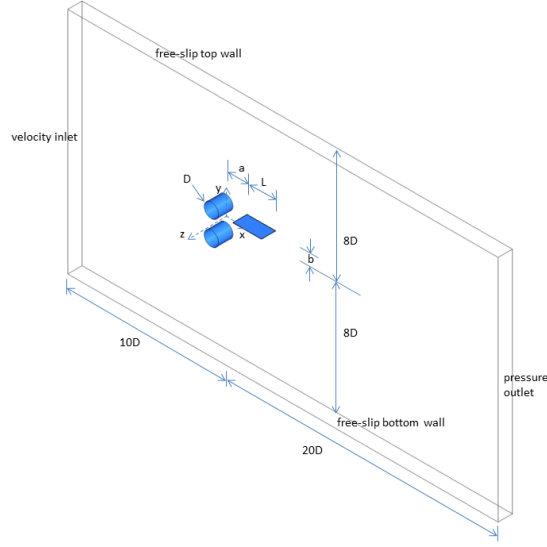
Figure 1: Computational domain and boundary conditions. Note that origin of x, y and z coordinate system is located centrally between the cylinder gap.

Table 1: Geometrical parameters

Parameters	Values	
cylinder diameter (D)	100 mm	
cylinder distance (T)	170 mm	$T/D = 1.7$
plate length (L)	200 mm	$L/D = 2$
plate thickness (h)	2 mm	
plate x-location (a)	$x/D = 0.5, 1.0, 1.5$	
plate y-location (b)	$y/D = -0.85, -0.425,$ $0, 0.425, 0.85$	

The physical parameters used for both the fluid and structure are compiled in Tables 2 and 3 respectively. Furthermore, a $T/D = 1.7$ in the biased flow regime is used. In doing so, we anticipate effects of interference or interactions between flow past side-by-side cylinders may be observed and analyzed. The flexible energy harvesting plate is made of a silicone rubber plate (elastic modulus $E = 13.1$ MPa, poisson ratio $\nu = 0.48$) with two layers of piezoelectric PVDF sheets (E = 2500 MPa, $\nu = 0.34$) attached along its top and bottom surfaces. The composite properties of this plate are summarized in Table 3.

Figure 2 illustrates the unstructured grids employed to discretize the fluid computational domain. A three-dimensional meshing scheme is used where finer meshing is prescribed in the vicinity of the two cylinders and flexible plate. In addition, denser grid points representing the boundary layer meshing is employed close to the surfaces of the cylinders and flexible plate, in order to better resolve their boundary layers. The first grid point normal to both cylinders and flexible plate in the boundary layer mesh were defined $0.001D$ away from their surfaces, maintaining maximum $y+ < 2$ in all simulation cases.

Table 2: Flow parameters in present study

Parameters	Values
inlet velocity (U_∞)	1.545 m/s
inlet turbulent intensity (I)	0.2%
outlet pressure	1 atm
Reynolds number (Re_D)	10000

Table 3: Structural parameters for plate

Parameters	Values
material density (ρ_s)	1780 kg/m^3
elastic modulus (E)	286.9 MPa
poisson ratio (ν)	0.346

As a result, depending on the simulation case - the baseline grid for the fluid domain consisted of 86847-95075 nodes (with 253243-291778 elements), while the plate was meshed using structured grids having 76 nodes (with 18 solid elements).

A commercial computational fluid dynamics and finite element solver (ANSYS Workbench 2019 R1) was employed to undertake the flow and structural modelling and coupling. The fluid-structural solver coupling was achieved using a partitioned framework, where the loads (from the fluid solver) were transferred to the structural solver (and applied to the plate) and the resulting plate deformation was feedback to the fluid solver to redefine the fluid domain (and corresponding mesh motion). A number of coupling iterations is typically required within each time step until convergence and a coupling under-relaxation factor of 0.75 was considered for both loads and displacements interchange, to closely couple the fluid-structure iterations. An implicit second order backward euler and Hilbert-Hughes-Taylor (HHT) schemes were used for time-integration of the discretized flow and structural equations respectively. Considering the vortex shedding frequencies of both cylinders and the flip-flopping period of the bistable gap flow that is several orders of magnitude greater than the vortex shedding period, a timestep size of 0.01s was used, which also showed adequate stability in the numerical iterations. The steady-state solution for a given stationary plate condition is used as the initial condition for all the unsteady fluid-structure simulation corresponding to each plate placement cases. Steady state flow condition was typically reached after non-dimensional time $tU_\infty/D = 75$ (corresponding to at least 15 vortex shedding periods) but were extended to run until $tU_\infty/D = 300$. Fluid-structure computations were then continued for a further $tU_\infty/D = 150$. Taking into account initial transients in the fluid-structure solutions, statistical results are presented by time-averaging quantities beyond overall $tU_\infty/D = 300$.

2.4 Simulation Cases

As vortex strength weakens further downstream of a cylinder, we considered a window in the wake region between $0.5 < x/D < 1.5$ and $-0.85 < y/D <$
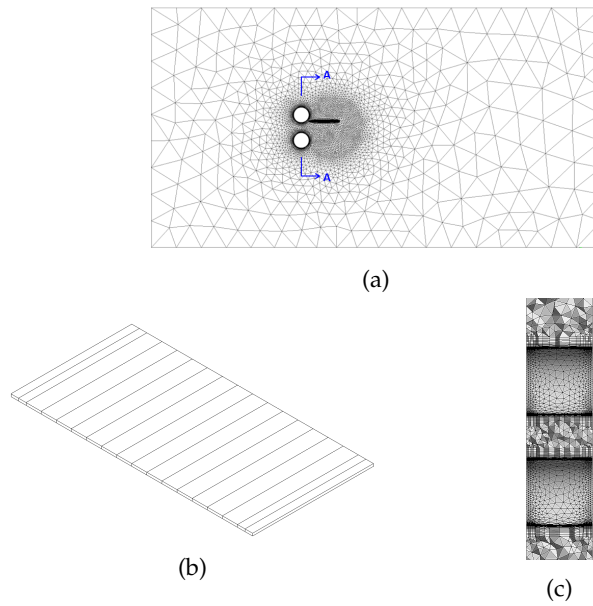
Figure 2: Baseline grids used in computational domain: (a) flow domain (b) structural domain (c) close-up of section A-A.

0.85 to place a flexible plate in the present study. In total, 15 cases were simulated corresponding to locations where leading edge of cantilever plate was fixed, as depicted in Figure 3. These cases are also tabulated in Table 6 highlighting their corresponding streamwise (x) and crossflow (y) coordinate positions.

2.5 Validation

A preliminary numerical simulation on two side-by-side cylinders at $Re_D = 6000$ and 10000 was firstly undertaken to verify the present modelling and meshing scheme. Table 4 summarizes comparison of present results against published numerical and experimental data from previous works.
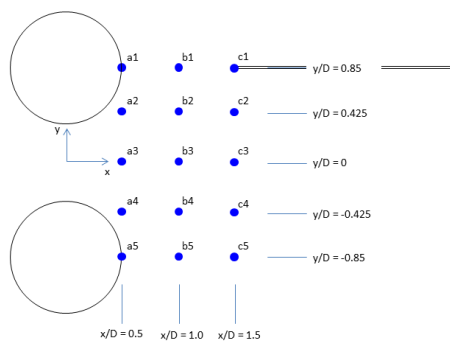

Figure 3: Placements of flexible plate leading edge (highlighted by blue dots) behind side-by-side cylinders and their corresponding case ID (labelled a1-c5).

Overall performance of the present model shows reasonable agreement with previous results based on their drag coefficients (C_d), lift coefficients (C_l) and Strouhal numbers (St). Considering differences in T/D, St in the present model indicates values within range of previous experiments performed at $T/D = 1.5, 2.0$ and numerical simulations at $T/D = 1.5, 1.75$. More importantly, the present model captures two distinct St indicating different vortex shedding periods corresponding to narrower and wider wakes in each cylinder, that is predominant in the biased flow regime. Consequently, this is also reflected in the distinct drag and lift coefficients reported for each cylinder in the present numerical model.

Table 4: Benchmarking with previous results at $Re_D = 6000$ and 10000 (* denotes data at $Re_D = 5000$ and subscripts '1' and '2' denotes upper and lower cylinder respectively)

	T/D	$Re_D = 6000$						$Re_D = 10000$					
		C_{d1}	C_{d2}	C_{l1}	C_{l2}	St_1	St_2	C_{d1}	C_{d2}	C_{l1}	C_{l2}	St_1	St_2
Present study	1.7	1.38	1.21	0.29	-0.23	0.28	0.19	1.31	1.10	0.29	-0.21	0.27	0.17
num. [34]	**1.5**	-	-	-	-	-	-	**1.32**	**1.34**	-	-	**0.20**	**0.20**
	1.75	-	-	-	-	-	-	**1.25**	**1.27**	-	-	**0.21**	**0.21**
num. [35]	1.5	-	-	-	-	-	-	1.36	1.32	-	-	-	-
num. [36]	2.0	-	-	-	-	-	-	1.37	1.37	0.22	-0.22	-	-
num. [3]	**1.7**	**1.21**		**-0.24**		-	-	-	-	-	-	-	-
exp. [3]	**1.7**	**1.06**		**-0.23**		-	-	-	-	-	-	-	-
exp. [7]	1.5	-	-	-	-	0.38	0.11	-	-	-	-	0.37	0.11
	2.0	-	-	-	-	0.26	0.18	-	-	-	-	0.22	0.22
exp.* [6]	1.75	-	-	-	-	0.32	0.15	-	-	-	-	-	-
exp. [37]	**1.7**	**1.12**	**0.84**	**0.18**	**-0.26**	-	-	**1.18**	**0.89**	**0.12**	**-0.14**	-	-
exp. [38]	1.5	-	-	-	-	-	-	1.29		-	-	0.20	

Although C_d and C_l in the present model are consistent with previous numerical studies (for example, $C_d = 1.21$ and $C_l = -0.24$ for $Re_D = 6000$ at $T/D = 1.7$ [3] and C_d between 1.25 to 1.32 for $Re_D = 10000$ at T/D between 1.5 and 1.75 [34], about which $T/D = 1.7$ in the present case falls within), the present numerical model overestimated their values in comparison to the experimental results in [37]. However, this difference in C_d and C_l with experimental results can be seen in all previous numerical studies reported in Table 4. This is potentially due to firstly, the difference in actual experimental to numerical conditions, and secondly, the difficulty in capturing flow separation using turbulence modelling in these sub-critical flow regimes, where the boundary layer remains laminar but the wake region is turbulent. Alternatively, comparison with [38] (albeit for $T/D = 1.5$) suggests closer agreement with experimental data.

In addition, while the present numerical model show biased gap flow pattern expected at this intermediate gap spacing [2, 38], previous numerical studies at $Re_D = 10000$ show symmetric unbiased flow. This may highlight the advantage of the present three-dimensional and Scale-Adaptive Simulation (SAS) turbulence model, which has been shown to better capture the unsteady fluctuations

under separated flow conditions than previous URANS turbulence models [31].

Further validation of the present model was performed by undertaking a grid- and time-independence test for flow past two side-by-side cylinders with a stationary plate placed behind the upper cylinder (corresponding to case a1 in Figure 3). A finer grid model (model B), where mesh size was effectively reduced by 1.6 to 2.0 - yielding a total of 226075 nodes in the fluid domain, was constructed. In addition, another simulation using the baseline grid model for case a1 but using a timestep size an order of magnitude lower (ie. model A with $\Delta t = 0.001s$) was undertaken. Table 5 shows small differences between the baseline model results and their corresponding finer grid model and smaller timestep simulation respectively - indicating that results in the present baseline model is sufficiently not sensitive to the size of the mesh and timestep.

Table 5: Comparison of flow parameters with models using finer grids (model B) and smaller timestep (model A) for case a1

	models		
	baseline	**model A**	**model B**
C_{d1}	1.002	1.003	1.004
C_{d2}	1.353	1.353	1.363
C_{l1}	0.123	0.123	0.157
C_{l2}	-0.325	-0.335	-0.350
St	0.050	0.052	0.055

3 Results and Discussion

Overall, 10-20 internal coupling iterations were necessary for fluid-structure coupling convergence at each time step. Computations for the initial stationary plate run may take up to 24 hours, while the following fluid-structure computations may run up to 45 hours, depending on the case simulated. We begin by presenting the oscillation history of the flexible plate when they are placed at each of the 15 locations highlighted in Figure 3. Plate tip displacements (in the y-direction) over time, when plate is positioned along various streamwise locations at each $-0.85 < y/D < 0.85$, are shown in Figure 4a - 4e. Tip oscillations show lowest amplitudes when flexible plate is placed along the centerline ($y/D = 0$) between the two side-by-side cylinders, compared to other y/D locations. Furthermore, their oscillating amplitude appears to be lowest when plate is closest to the cylinders ($x/D = 0.5$) before maximizing at $x/D = 1.0$ and decreases as the plate is placed further downstream, as shown in Figure 4c. In order to better quantify plate vibration behaviour behind the cylinders, the mean y-displacements ($\bar{y}$) of the tip was calculated for each case. In addition, as piezoelectric effect is affected by their mechanical strains, which occur irrespective of positive or negative direction in plate deflection, we considered taking their vibration amplitude (A) over time and calculated their root-mean-square (A_{rms}) as an indication of the overall level in mechanical strains experienced by the piezoelectric beam (and hence, energy harvesting potential), for all 15 cases.

Table 6 summarizes these $\bar{y}$ and A_{rms} values for all the cases simulated in the present study. Inspecting the table, a number of observations may be hy-

pothesized in regards to variation in $\overline{y}$ and A_{rms} with respect to plate placement in the wake region:

1. The mean y-displacements $\overline{y}$ shows opposing deflections between plate positioned above and below the centerline $y/D = 0$. At locations immediately behind both cylinders (ie. $x/D = 0.5$), plate placed above the centerline ($y/D > 0$) tended to oscillate about a mean position that is deflected downwards ($\overline{y} < 0$), while plate placed below the centerline ($y/D < 0$) tended to oscillate about a mean position that deflects upwards ($\overline{y}>0$). However, away from the cylinders (ie. $x/D = 1.0.1.5$), the opposite occurs, where plate positioned above the centerline appears to oscillate about a mean position that is deflected upwards (ie. $\overline{y}>0$) and plate positioned below the centerline appears to deflect more downwards (ie. $\overline{y}<0$).

2. In the vicinity immediately behind the cylinders (ie. $x/D = 0.5$), putting the flexible plate on the rear center point of either cylinders (ie. $y/D = 0.85, -0.85$) is found to promote highest overall plate oscillations (ie. indicated by maximum A_{rms}). However, further downstream from both cylinders (ie. $x/D = 1.0, 1.5$) placing the flexible plate at intermediate region above or below the centerline $y/D = 0$ (ie. at $y/D = 0.425$ and $y/D = -0.425$) is shown to generate highest overall amplitudes in plate oscillations along their respective streamwise positions.

3. Flexible plate placed along the centerline $y/D = 0$ show the lowest root-mean-square in their oscillation amplitude. Furthermore, root-mean-square in amplitude of plate oscillation with respect to their placement behind two side-by-side cylinders appear to be mirrored about the centerline $y/D = 0$ (ie. A_{rms} at $y/D = 0.85$ are closer in values to A_{rms} at $y/D = -0.85$, and A_{rms} at $y/D = 0.425$ are closer in values to A_{rms} at $y/D = -0.425$) along a streamwise location. This is further evident from the contour plot showing distribution of A_{rms} behind both cylinders, depicted in Figure 5.

Figure 5 shows the variation in root-mean-square of the oscillation amplitude (A_{rms}) with respect to plate placement behind two side-by-side cylinders. The contours were generated from the results at the 15 locations in Table 6 using a cubic spline interpolation, giving predicted A_{rms} for the flexible plate if they are located along various (x/D, y/D) locations behind the two cylinders. Thus, Figure 5 indicates potential locations where flexible plate may be placed to undergo high overall vibration amplitudes. This include rear center points on either cylinders or in the intermediate region off-center from the centerline between the cylinders (for placements further downstream). Overall maximum mean amplitude of oscillation is recorded when flexible plate is placed at $x/D = 1.5, y/D = -0.425$ (ie. case c4), where their mean amplitude is almost twice the mean amplitude on the centerline at similar streamwise (x) position. Figure 6a-6c highlights spanwise vorticity contour plot corresponding to cases with maximum mean amplitude for each streamwise locations $x/D = 0.5, 1.0, 1.5$. While biased flow regime (with narrow and wide asymmetric wake patterns behind either cylinders) is expected to take place for side-by-side cylinders in the present $T/D = 1.7$, it is found that this wake pattern still persists in the presence
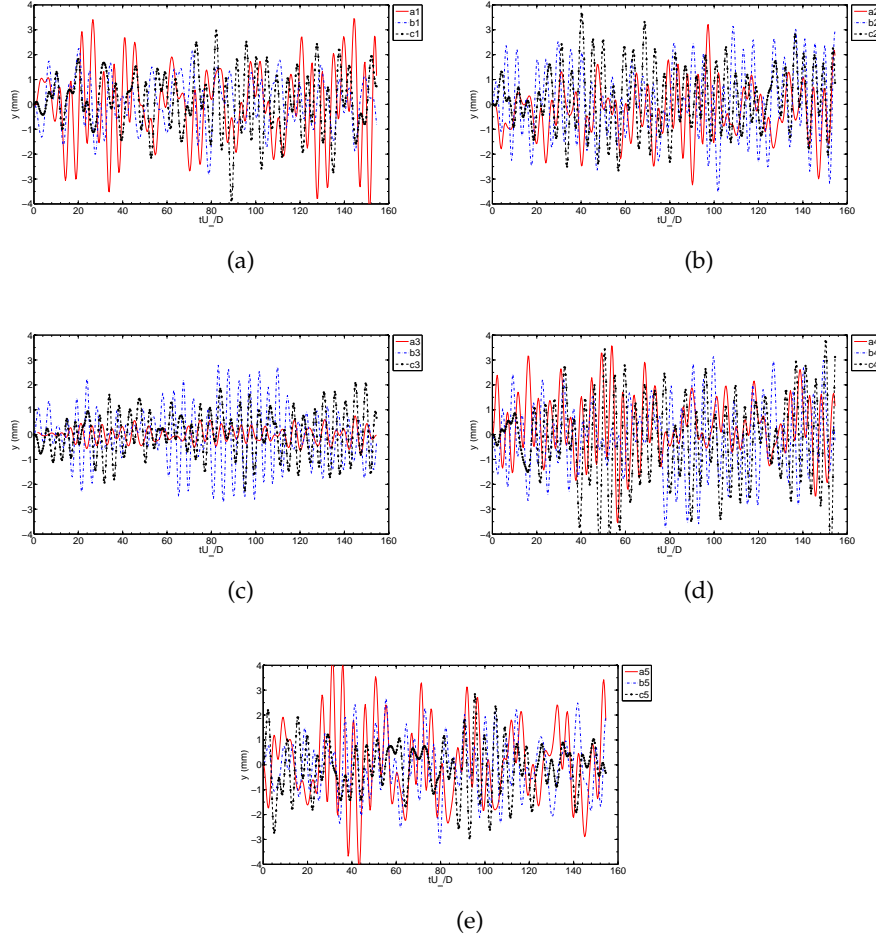
(a)

(b)

(c)

(d)

(e)

Figure 4: Plate tip y-displacements for plate positioned at $x/D = 0.5, 1.0, 1.5$ (denoted by case numbers in each chart legend) at several y/D locations: (a) $y/D = 0.85$ (b) $y/D = 0.425$ (c) $y/D = 0$ (d) $y/D = -0.425$ (e) $y/D = -0.85$. Note that the solid red lines represent cases at $x/D = 0.5$, dashed-dotted blue lines represent cases at $x/D = 1.0$ and black dashed lines with circle markers represent cases at $x/D = 1.5$.

of a flexible plate. Comparing at instances when their respective plate amplitude is maximum, the narrow-wide wake pattern is more pronounced for cases b2 and c2 (ie. Figure 6b and 6c), where plate is placed at $y/D = \pm0.425$, compared to case a5 where plate is placed centrally behind a cylinder at $y/D = -0.85$. In contrast, the wake pattern for case a3 (corresponding to lowest mean amplitude case located along centerline $y/D = 0$) in Figure 6d, shows minimal difference in wake size between cylinders, highlighting (i) potential suppression of biased gap flow when flexible plate is centrally positioned and close to both cylinders (similar to previous study in Oruc et al. [20] but with plate length not extending upstream in the present study) and (ii) important role of biased gap flow on plate vibrations behind two side-by-side cylinders. Consequently, wake-excited

12

Table 6: Mean of plate displacement and root-mean-square of oscillating amplitude against plate location

Case ID	Location		Results	
	x/D	y/D	$\bar{y}$ (mm)	A_{rms} (mm)
a1		0.85	-0.037	1.514
a2		0.425	-0.309	1.031
a3	0.5	0	-0.012	0.283
a4		-0.425	0.343	1.193
a5		-0.85	0.068	1.551
b1		0.85	0.079	0.960
b2		0.425	0.053	1.417
b3	1.0	0	-0.057	1.133
b4		-0.425	-0.157	1.412
b5		-0.85	-0.027	1.129
c1		0.85	0.124	1.142
c2		0.425	0.251	1.230
c3	1.5	0	0.017	0.856
c4		-0.425	-0.248	1.618
c5		-0.85	-0.112	0.999
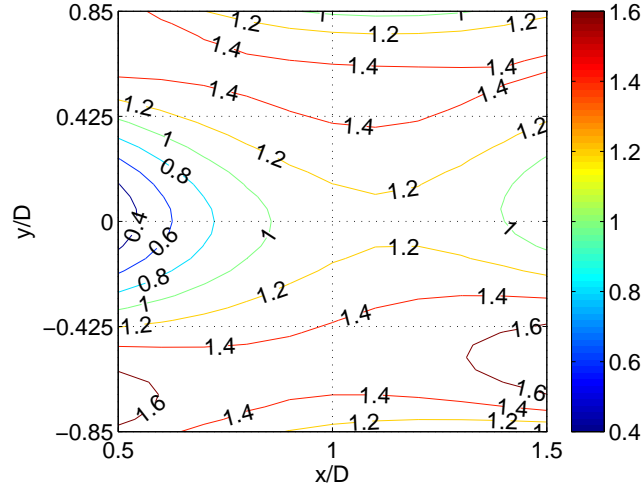
Figure 5: Contours representing root-mean-square of plate oscillation amplitudes (A_{rms}) behind two side-by-side cylinders.

energy harvesting plate may be positioned away from the centerline $y/D = 0$ to maximize their energy output for this type of bluff body configuration.

4   Conclusion

Wake-excited vibrations of a flexible plate behind two side-by-side cylinders was computationally investigated in their biased flow regime at $Re_D = 10000$.
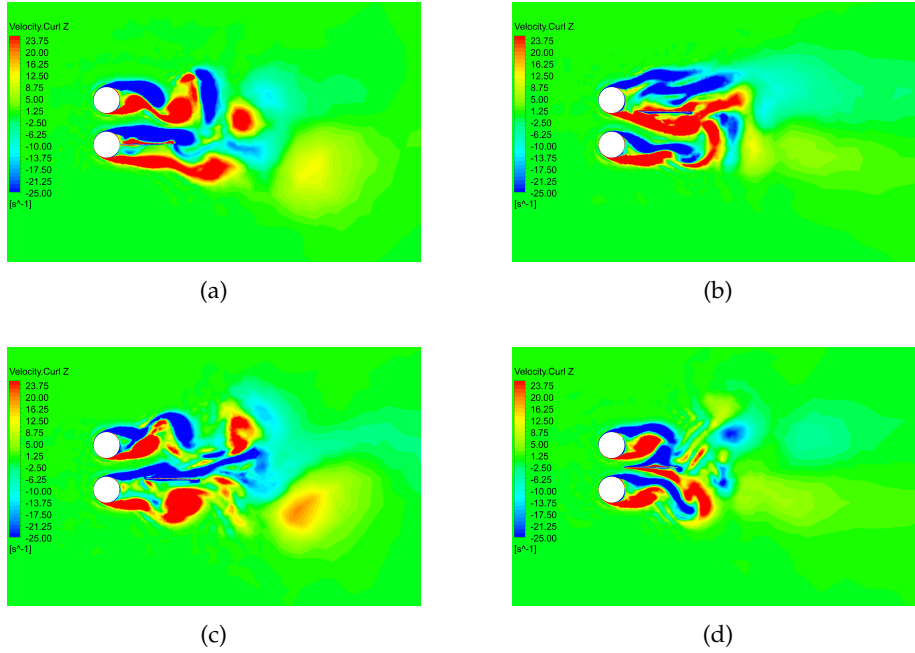
Figure 6: Contour of spanwise vorticity at instance when plate exhibit maximum amplitude for: (a) case a5 (b) case b2 (c) case c4 (d) case a3.

Using a Scale-Adaptive SST turbulence flow model and partitioned coupling to a finite element solver, vibration response of a flexible plate placed at various locations in the wake region were simulated and analyzed. Numerical results indicate placing flexible plate along centerline between both cylinders generated low mean amplitude of oscillations and may potentially suppress biased gap flow if positioned close to both cylinders. It was found that plate vibrations are maximized when placed immediately behind either cylinders or further downstream within some intermediate region off-center from the centerline, where biased asymmetric wake interactions are present. These numerical findings may be exploited to identify favourable placements to maximize wake-excited energy harvesters behind side-by-side circular cylindrical structures. It is remarked that the present study had focused on $Re_D = 1000$, biased flow regime $T/D = 1.7$ and wake region within $0.5 < x/D < 1.5$ and $-0.85 < y/D < 0.85$. Future simulations at various other Re_D, T/D and wider region behind both cylinders are anticipated, to further understand effects of Re_D, T/D and other plate positioning on their vibration and energy harvesting potential.

Author Contributions

Funding

Acknowledgments

Conflicts of Interest

The authors declare no conflict of interest. The funders had no role in the design of the study; in the collection, analyses, or interpretation of data; in the writing of the manuscript, or in the decision to publish the results.

Abbreviations

The following abbreviations are used in this manuscript:

A	amplitude of plate oscillation
A_{rms}	root-mean-square of plate oscillation amplitude
c	damping ratio of plate
C_d	coefficient of drag
C_l	coefficient of lift
d	vector of plate displacements (m)
D	cylinder diameter (m)
E	plate Young's modulus (N/m^2)
f	external force vector applied on plate (N)
f_n	plate natural frequency (Hz)
h	plate thickness (m)
I	turbulent intensity (%)
L	plate length (m)
p	pressure (N/m^2)
Re	Reynolds number
Re_D	Reynolds number based on diameter
St	Strouhal number
St_n	Strouhal number of narrow wakes
St_w	Strouhal number of wide wakes
t	time (s)
T	center-to-center cylinder spacing (m)
u_i	fluid velocities (m/s)
$\widetilde{u}_j$	grid velocity (m/s)
U_∞	incoming free-stream velocity (m/s)
x_i	space or direction vectors (m)
$\overline{y}$	mean of plate displacement (m)
$y+$	dimensionless first grid normal distance to wall
Δt	timestep size (s)
μ	fluid dynamic viscosity (Pa.s)
μ_t	turbulence eddy viscosity (Pa.s)
ν	poisson ratio
ρ	fluid density (kg/m^3)
ρ_s	structural or plate density (kg/m^3)
σ_{ij}	plate stress tensor (N/m^2)
ALE	Arbitrary Eulerian-Lagrangian
PVDF	Polyvinylidene Fluorides
RANS	Reynolds Averaged Navier-Stokes
SAS	Scale-Adaptive Simulationn
URANS	Unsteady Reynolds Averaged Navier-Stokes

References

[1] Zhou, Y. and M. M. Alam (2016). Wake of two interacting circular cylinders: A review. *International Journal of Heat and Fluid Flow 62*, 510 – 537.

[2] Sumner, D. (2010). Two circular cylinders in cross-flow: A review. *Journal of Fluids and Structures 26*(6), 849 – 899.

[3] Atkins, M. D., L. Dala, and T. Kim (2016). Time-averaged behavior of gap flow between two side-by-side circular cylinders. *AIAA Journal 54*(9), 2742–2754.

[4] Zdravkovich, M. (1987). The effects of interference between circular cylinders in cross flow. *Journal of Fluids and Structures 1*(2), 239 – 261.

[5] Spivack, H. M. (1946). Vortex frequency and flow pattern in the wake of two parallel cylinders at varied spacing normal to an air stream. *Journal of the Aeronautical Sciences 13*(6), 289–301.

[6] Song, F.-L., S.-Y. Tseng, S.-W. Hsu, and C.-H. Kuo (2015). Gap ratio effect on flow characteristics behind side-by-side cylinders of diameter ratio two. *Experimental Thermal and Fluid Science 66*, 254 – 268.

[7] Zhou, Y., S. X. Feng, M. M. Alam, and H. L. Bai (2009). Reynolds number effect on the wake of two staggered cylinders. *Physics of Fluids 21*(12), 125105.

[8] Xu, S. J., Y. Zhou, and R. M. C. So (2003). Reynolds number effects on the flow structure behind two side-by-side cylinders. *Physics of Fluids 15*(5), 1214–1219.

[9] Liu, C., Y.-y. Gao, X.-c. Qu, B. Wang, and B.-f. Zhang (2019, Jun). Numerical simulation on flow past two side-by-side inclined circular cylinders at low reynolds number. *China Ocean Engineering 33*(3), 344–355.

[10] Chehreh, B. B. and K. Javadi (2018). Flow control around a circular cylinder with swinging thin plates. *Journal of Fluids and Structures 81*, 738 – 760.

[11] Vu, H. C., J. Ahn, and J. H. Hwang (2016, Sep). Numerical investigation of flow around circular cylinder with splitter plate. *KSCE Journal of Civil Engineering 20*(6), 2559–2568.

[12] Teksin, S. and S. Yayla (2016.). Effects of flexible splitter plate in the wake of a cylindrical body. *Journal of Applied Fluid Mechanics 9*(6), 3053–3059.

[13] Wu, J., C. Shu, and N. Zhao (2014). Numerical study of flow control via the interaction between a circular cylinder and a flexible plate. *Journal of Fluids and Structures 49*, 594 – 613.

[14] Abdi, R., N. Rezazadeh, and M. Abdi (2019). Investigation of passive oscillations of flexible splitter plates attached to a circular cylinder. *Journal of Fluids and Structures 84*, 302 – 317.

[15] Wang, H., Q. Zhai, and J. Zhang (2018). Numerical study of flow-induced vibration of a flexible plate behind a circular cylinder. *Ocean Engineering 163*, 419 – 430.

[16] Yu, Y. and Y. Liu (2015). Flapping dynamics of a piezoelectric membrane behind a circular cylinder. *Journal of Fluids and Structures 55*, 347 – 363.

[17] Shi, S., T. New, and Y. Liu (2013). Flapping dynamics of a low aspect-ratio energy-harvesting membrane immersed in a square cylinder wake. *Experimental Thermal and Fluid Science 46*, 151 – 161.

[18] Furquan, M., T. R. Sahu, and S. Mittal (2017, apr). Numerical simulation of vortex induced vibration of cylinders with flexible splitter plates. *Journal of Physics: Conference Series 822*, 012078.

[19] Octavianty, R. and M. Asai (2016). Effects of short splitter plates on vortex shedding and sound generation in flow past two side-by-side square cylinders. *Experiments in Fluids 57:143*, 1–13.

[20] Oruc, V., M. A. Akar, H. Akilli, and B. Sahin (2013). Suppression of asymmetric flow behavior downstream of two side-by-side circular cylinders with a splitter plate in shallow water. *Measurement 46*(1), 442 – 455.

[21] Allen, J. and A. Smits (2001). Energy harvesting eel. *Journal of Fluids and Structures 15*(3), 629 – 640.

[22] An, X., B. Song, W. Tian, and C. Ma (2018). Design and cfd simulations of a vortex-induced piezoelectric energy converter (vipec) for underwater environment. *Energies 11*(2).

[23] Shan, X., R. Song, M. Fan, and T. Xie (2016). Energy-harvesting performances of two tandem piezoelectric energy harvesters with cylinders in water. *Applied Sciences 6*(8).

[24] Goushcha, O., H. Akaydin, N. Elvin, and Y. Andreopoulos (2015). Energy harvesting prospects in turbulent boundary layers by using piezoelectric transduction. *Journal of Fluids and Structures 54*, 823 – 847.

[25] Akaydın, H. D., N. Elvin, and Y. Andreopoulos (2010, Jul). Wake of a cylinder: a paradigm for energy harvesting with piezoelectric materials. *Experiments in Fluids 49*(1), 291–304.

[26] Weinstein, L. A., M. R. Cacan, P. M. So, and P. K. Wright (2012). Vortex shedding induced energy harvesting from piezoelectric materials in heating, ventilation and air conditioning flows. *Smart Materials and Structures 21*, 045003. available online http://dx.doi.org/10.1088/0964-1726/21/4/045003.

[27] Nguyen, H.-D. T., H.-T. Pham, and D.-A. Wang (2013). A miniature pneumatic energy generator using kármán vortex street. *Journal of Wind Engineering and Industrial Aerodynamics 116*, 40–48. available online http://dx.doi.org/10.1016/j.jweia.2013.03.002.

[28] Menter, F. R. and Y. Egorov (2010, Jul). The scale-adaptive simulation method for unsteady turbulent flow predictions. part 1: Theory and model description. *Flow, Turbulence and Combustion 85*(1), 113–138.

[29] ANSYS Inc. (2016). *ANSYS CFX Solver Theory Guide - Release 17.*

[30] Donea, J., A. Huerta, J.-P. Ponthot, and A. Rodriguez-Ferran (2004). Arbitrary lagrangian-eulerian methods. In *Encyclopedia of Computational Mechanics*. John Wiley & Sons.

[31] Jadidi, M., F. Bazdidi-Tehrani, and M. Kiamansouri (2018). Scale-adaptive simulation of unsteady flow and dispersion around a model building: spectral and pod analyses. *Journal of Building Performance Simulation 11*(2), 241–260.

[32] Alkishriwi, N., M. Meinke, and W. Schroder (2006). A large-eddy simulation method for low mach number flows using preconditioning and multigrid. *Computers & Fluids 35*, 1126–1136.

[33] Shen, Y., G. Zha, and B. Wang (2008, 23 - 26 June 2008, Seattle, Washington). Large eddy simulation of circular cylinder flow by using high order WENO scheme. In *38th Fluid Dynamics Conference and Exhibit*, Seattle, Washington, pp. AIAA 2008–3748.

[34] Li, D., Q. Yang, X. Ma, and G. Dai (2018). Free surface characteristics of flow around two side-by-side circular cylinders. *Journal of Marine Science and Engineering 6*(3).

[35] Jun, L. and J. Sirui (2001). Numerical simulation of flow around two cylinders at high reynolds number. *Journal of Hydrodynamics 16*, 101–109.

[36] Sarvghad-Moghaddam, H., N. Nooredin, and B. Ghadiri-dehkordi (2011). Numerical simulation of flow over two side-by-side circular cylinders. *Journal of Hydrodynamics, Ser. B 23*(6), 792 – 805.

[37] Zhou, Y., Z. J. Wang, R. M. C. So, S. J. Xu, and W. Jin (2001). Free vibrations of two side-by-side cylinders in a cross-flow. *Journal of Fluid Mechanics 443*, 197–229.

[38] Bearman, P. W. and A. J. Wadcock (1973). The interaction between a pair of circular cylinders normal to a stream. *Journal of Fluid Mechanics 61*(3), 499–511.